Journal of Petroleum Science and Engineering 62 (2008) 1–15

Contents lists available at ScienceDirect

Journal of Petroleum Science and Engineering

journal homepage: www.elsevier.com/locate/petrol

A study to assess the value of post-stack seismic amplitude data in forecasting fluid production from a Gulf-of-Mexico reservoir

Maika Gambús-Ordaz, Carlos Torres-Verdín *

The University of Texas at Austin, USA

ARTICLE INFO

Article history:
Received 17 July 2006
Accepted 13 June 2008

Keywords:
geostatistical inversion
reservoir simulation
post-stack seismic amplitude data
integrated reservoir characterization

ABSTRACT

This paper describes a study undertaken to appraise the reliability of spatially complex hydrocarbon reservoir models constructed with the use of post-stack seismic amplitude data and well logs. Developments center about the interpretation of data acquired in an active hydrocarbon field in the Gulf of Mexico. The availability of measured time records of fluid production and pressure depletion provides an independent way to quantify the accuracy and reliability of several methods commonly employed to construct static reservoir models. We make use of geostatistical inversion to construct spatial distributions of porosity and permeability that simultaneously honor well logs and post-stack seismic amplitude data. The constructed reservoir models are compared against models constructed with conventional geostatistical procedures that do not make use of seismic amplitude data or else that use a simple statistical correlation between petrophysical properties and seismic-inverted acoustic impedances.

We perform multi-phase fluid-flow simulations to assess the consistency of the constructed reservoir models against the measured time record of flow rates of gas/water and shut-in well pressures. For the hydrocarbon field under consideration, the joint stochastic inversion of well logs and post-stack seismic amplitude data yields the closest match to dynamic measurements of fluid production and pressure depletion. We found that the spatial continuity of permeability exhibited the largest influence on the behavior of fluid production and pressure depletion with time. Perturbations to the relationships between porosity, permeability, and acoustic impedance produced significant variations in the simulated time record of fluid production. Finally, we found that the degree of spatial variability of permeability and porosity, and presence of permeability anisotropy were substantially more significant in the prediction of fluid production than variability of relative permeability and capillary pressure.

1. Introduction

The central goal of reservoir characterization is to provide quantitative static and dynamic descriptions of a reservoir. To accomplish this goal, measurements acquired at different locations in the reservoir, with different lengths of spatial resolution, and obeying different physical principles, are integrated in a manner that is consistent with a geological framework. A large uncertainty in much of the data available to forecast reservoir performance stems from the fact that, in general, stratigraphic sequences exhibit a high degree of spatial variability. In addition, because of the high cost associated with the acquisition of subsurface measurements, fundamental petrophysical parameters such as permeability and porosity are usually measured/estimated only at a few locations. Laboratory measurements of rock-fluid properties such as irreducible water saturation, wettability, capillary pressure, and relative permeability are even scarcer given their high cost and low reliability. The combination of significant spatial heterogeneity with a relatively sparse and small number of measurements leads to uncertainty about the values of inter-well petrophysical properties and, therefore, to uncertainty in predicting fluid production with time. Such an adverse situation is exacerbated by the nonlinear nature of multi-phase fluid displacement in porous media governing fluid production and pressure depletion in hydrocarbon reservoirs.

This paper describes a methodology to construct spatial distributions of porosity and permeability constrained by post-stack seismic amplitude data and applied to a gas/condensate- and oil-producing field. We pursue two specific objectives:

(1) To quantitatively integrate seismic amplitude data in the construction of static reservoir models and to assess the impact of such integration in the prediction of dynamic reservoir behavior after the onset of production.
(2) To quantify the effect of uncertainty in rock-fluid parameters on the predicted time record of fluid production, especially in relation to uncertainty in the spatial distribution of porosity and permeability.

* Corresponding author.
E-mail addresses: mkgambus@yahoo.com (M. Gambús-Ordaz), cverdin@mail.utexas.edu (C. Torres-Verdín).

0920-4105/$ – see front matter © 2008 Elsevier B.V. All rights reserved.
doi:10.1016/j.petrol.2008.06.001

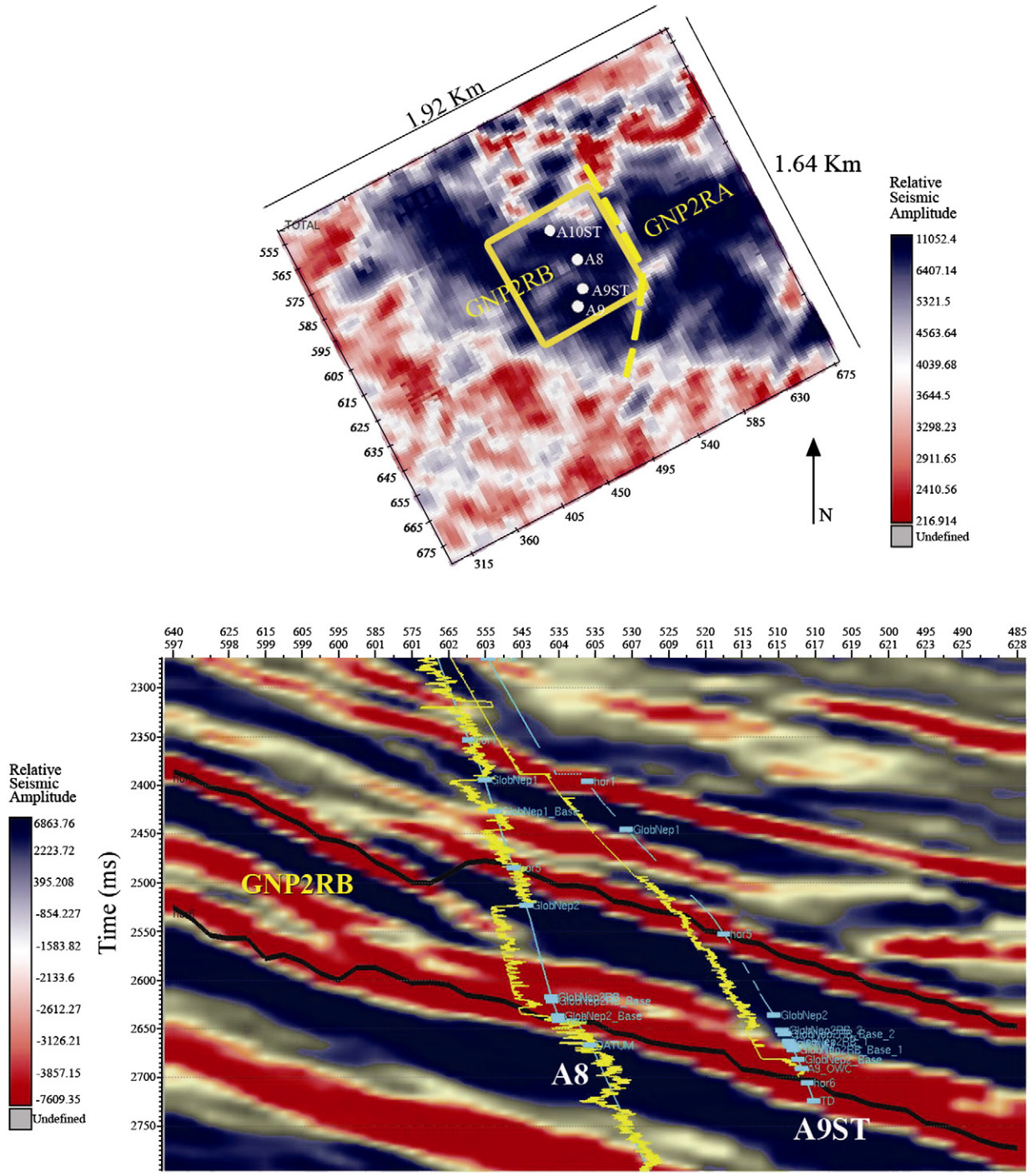

Fig. 1. Plan view of the spatial coverage of the available 3D post-stack seismic data. Upper panel: well locations (four, shown in white), superimposed to a color-coded seismic RMS (root-mean-square) amplitude map extracted within the seismic-time bounds of the main sand reservoir (GNP2RB). Dark blue and red describe high and low RMS seismic amplitudes, respectively. The dashed-yellow lines indicate the location of the sealing fault that divides the GNP2RA and GNP2RB reservoirs. A yellow rectangle describes the area subject to numerical simulation of fluid production measurements. Lower panel: cross-section of the post-stack seismic data showing the trajectories (light blue) and gamma-ray logs (in yellow) of two of the wells (A8 and A9ST) that penetrate the GNP2RB reservoir. The black lines describe seismic horizons that define the upper and lower boundaries of the GNP2RB reservoir.

To accomplish the above objectives, we consider three different statistical procedures to construct spatial distributions of reservoir porosity and permeability, namely:

(a) sequential Gaussian simulation honoring well-logs,
(b) collocated sequential Gaussian co-simulation honoring well-logs and linear correlations between seismic-inverted acoustic impedance and both porosity and logarithm of permeability, and
(c) a geostatistical inversion procedure that simultaneously honors both 3D seismic amplitude data and well logs.

Journel and Huijbregts (1978) published the first sound work to honor simultaneously well logs and seismic amplitude data under a geostatistical framework. However, it was Haas and Dubrule (1994) who first provided a complete technical description of the method and who first presented experimental validation results. Pendrel and Van

Riel (1997) described an application of geostatistical inversion to estimate inter-well porosity and to quantify uncertainty of their estimations. Subsequently, Grijalba-Cuenca et al. (2000) described a methodology to generate independent stochastic realizations of lithology and density indirectly linked to acoustic impedance.

Geostatistical methods are often used to construct static reservoir models. However, these methods do not explicitly honor dynamic measurements such as oil and gas production. Landa and Horne (1997) described a mathematical procedure to estimate reservoir distributions of porosity and permeability indirectly linked to seismic amplitude data and dynamic fluid production measurements. Nevertheless, permeability distributions were computed deterministically based on the assumption of a linear relationship between porosity and logarithm of permeability. More recently, Varela et al. (2002) developed a global inversion algorithm for the estimation of inter-well elastic and petrophysical parameters using pre-stack seismic amplitude data and well logs. However, their algorithm was validated and tested only on synthetic data.

In this paper, we make use of the three strategies described earlier to construct stochastic realizations of spatial distributions of porosity and permeability. Subsequently, these realizations are subject to numerical simulation of multiphase fluid flow to assess their agreement with the measured time records of fluid production and pressure depletion. Rock-fluid and fluid properties are assumed the same for all of the cases. Therefore, discrepancies in the numerically simulated fluid production are attributed to the procedure employed to populate porosity and permeability in the inter-well region. Finally, we assess the variability and reliability of the constructed reservoir models by systematically quantifying the relative influence of the assumed seismic-petrophysical correlation parameters and rock-fluid properties on the simulated time records of fluid production and pressure depletion.

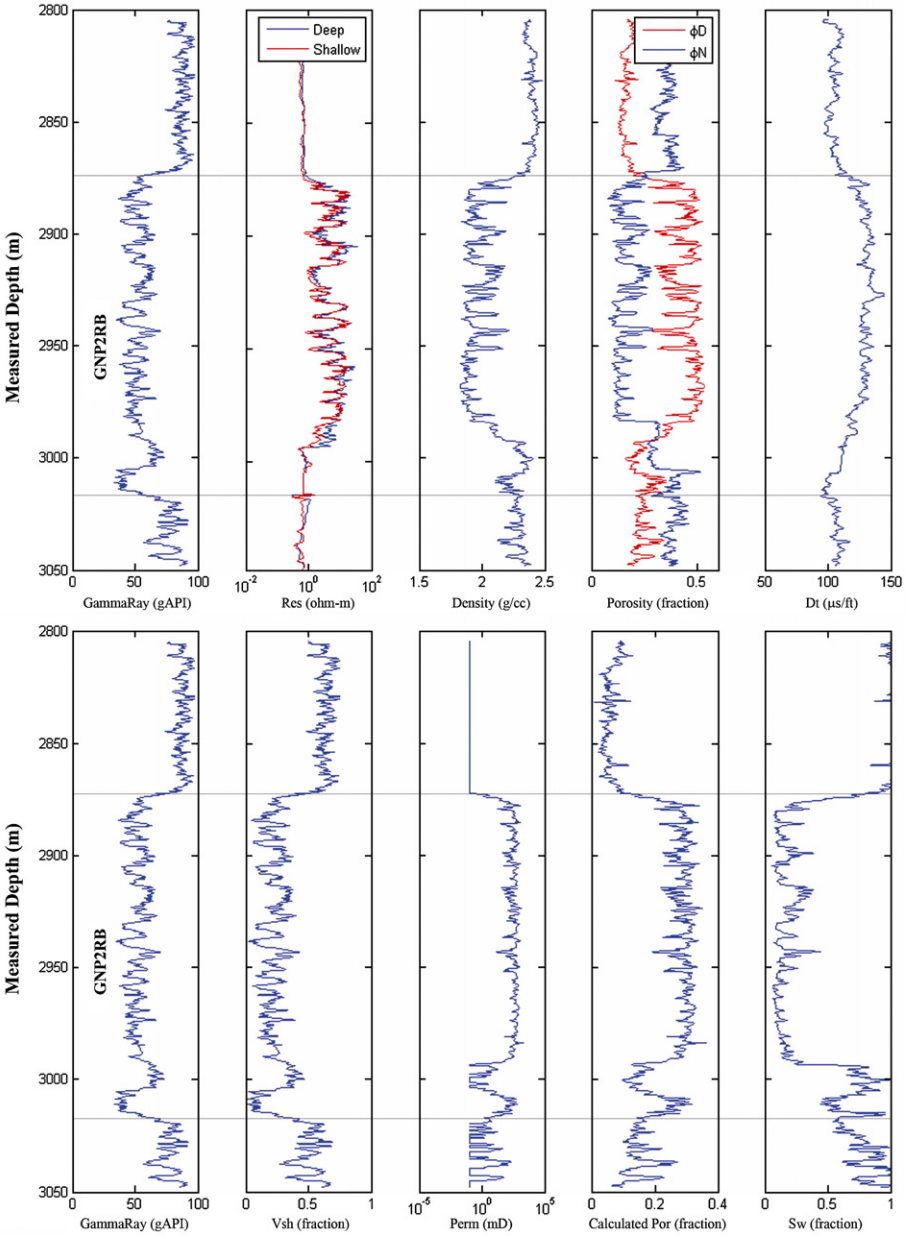

Fig. 2. Description of well-log measurements in well A8 and their petrophysical interpretation across the GNP2RB reservoir. From left to right, the upper panels describe the gamma ray, deep and shallow resistivity, density-neutron porosity, and P-wave slowness logs. The lower panels describe, from left to right, the gamma-ray log, the calculated shale volume, the calculated permeability, the calculated porosity, and the calculated water saturation.

2. The data set and petrophysical analysis

2.1. The data set

The upper panel of Fig. 1 is a plan view of the spatial coverage of the post-stack seismic data. Well locations are overlain on a color-coded seismic RMS (root-mean-square) amplitude map calculated across the main flow unit in the reservoir. The areal coverage on that figure is 3.14 km^2, included in a 6.25 km × 3.99 km seismic cube. A total of 183 cross-lines and 122 inlines constitute the available seismic data over the area of study. The post-stack seismic data consist of traces sampled at 4 ms in the frequency band between 5 and 80 Hz, with a central frequency of 28 Hz.

The zone of interest is located between 2700 m and 3100 m below the sea bottom (the average seawater column is 54 m). A sealing fault separates the two segments of the main flow units in the reservoir, here referred to as GNP2RA and GNP2RB. Our study is focused on the west side of the fault that limits the GNP2RB reservoir. A total of 36 cross-lines and 15 in-lines constitute the available data set over an area of approximately 162,000 m^2 that includes the GNP2RB reservoir. The bottom panel of Fig. 1 shows the locations of two of the wells (A8 and A9ST) superimposed on a cross-section of the 3D post-stack seismic amplitude data. In that figure, black lines identify the intersection of the two seismic horizons that mark the lower and upper boundaries of the GNP2RB reservoir.

Fig. 2 is a composite well-log display of wireline data acquired along well A8. The upper panels in that figure show, from left to right, the gamma ray log, the deep and shallow resistivity logs, the density log, the density and neutron porosity logs, and the compressional sonic log across the GNP2RB reservoir. Gas-bearing flow units are readily identified from the crossover between the density and neutron porosity logs. From well-log measurements, it is found that the average P-wave velocity is approximately 2562 m/s, whereupon the tuning wavelength is approximately equal to 23 m. Fig. 2 shows that the average thickness of individual sand units is approximately 153 m. Since the thickness of the vertical hydrocarbon column ranges between 335 m and 396 m, it becomes clear that post-stack seismic amplitude data have the vertical resolution necessary to identify individual sand units.

Exploration targets are Lower Pliocene upper slope sands interpreted as amalgamated channel deposits flanked by a salt dome. Reservoir sands are unconsolidated and amalgamated turbidite deposits, most likely ponded in an interslope basin on the southern flank of the salt dome. The reservoir is a structural closure with bounding faults radiating out from the salt dome. Due to the proximity of the salt dome, reservoir sands exhibit dip angles of up to 27° thereby making seismic amplitude preservation and well ties considerably difficult. Two exploratory wells and sixteen development wells were drilled after the initial discovery; however, only two of them, A8, and A9ST, were completed across the GNP2RB reservoir.

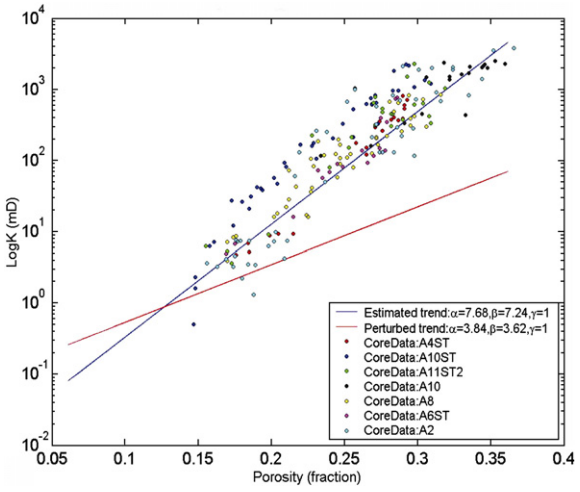

Fig. 3. Cross-plot of porosity and logarithm of permeability constructed with rock-core measurements. The solid blue line describes the linear trend inferred from multi-linear regression analysis, while the solid red line describes a 50%-perturbation trend used to assess the effect of the linear correlation on the simulated time records of fluid production and pressure depletion (Sensitivity Analysis No. 3; refer to case GI-5 in Table 2).

2.2. Petrophysical analysis

In order to estimate petrophysical properties such as porosity, permeability, and water saturation in the GNP2RB reservoir, we performed standard calculations on the available well logs.

An iterative procedure between density porosity, neutron porosity, and fluid saturations (gas, oil, and water) was used to calculate the total porosity that agreed with rock-core porosity measurements (Gambús, 2005). The calculated porosity was derived assuming presence of sand, shale, and fluids. We used the Simandoux equation (Bassiouni, 1994) to calculate water saturation. Pickett plots (Bassiouni, 1994) indicated that the electrical resistivity of connate water was approximately equal to 0.017 Ω-m. To estimate well-log permeability, we assumed a relationship between porosity and irreducible water saturation similar to that of Tixier and Timur (Balan et al., 1995). Rock-core measurements were available to calibrate the estimation of permeability. The mathematical expression for permeability assumes that rocks remain at irreducible water saturation and is given by

$$k = \gamma \frac{\phi^{\alpha}}{S_{\mathrm{wi}}^{\beta}}, \tag{1}$$

where γ, α, and β are parameters calculated with a multi-linear regression analysis of rock-core laboratory measurements. In Eq. (1), k is the calculated permeability and S_{wi} is irreducible water saturation, here assumed constant and equal to 12%. The lower panels in Fig. 2 show, from left to right, the gamma ray log, the calculated shale volume, the calculated permeability, the calculated porosity, and the calculated water saturation across the GNP2RB reservoir.

Fig. 3 is a cross-plot of porosity and logarithm of permeability. In that figure, the solid blue line represents the linear trend estimated from multi-linear regression analysis of the rock-core measurements, whereas the colored points correspond to actual rock-core measurements. The solid red line in the same figure is included as reference and describes a 50%-perturbation of the rock-core trend to be subsequently used in this paper for sensitivity analysis.

3. Seismic-inverted acoustic impedance and its relationship to petrophysical parameters

While the analysis and interpretation of seismic amplitudes have great merit, it is difficult to integrate them directly into reservoir models for engineering purposes, such as for flow simulations and volumetric calculations. Therefore, a method is required for converting aggregate seismic amplitude responses into layer properties. Such a method is referred to as seismic inversion (Bashore et al., 1993); it consists of estimating acoustic impedance (the product of bulk density and P-wave velocity) from variations of seismic amplitude as a function of vertical travel time.

The first step in seismic inversion is to estimate the source wavelet. We estimated seismic wavelets with synthetic seismograms for each of the two wells that included acoustic impedance measurements across and below the GNP2RB reservoir. Given the close match between the two independently estimated wavelets, the relative proximity of the two wells, and the high similarity between the two local seismic amplitude spectra involved, we opted to use the average of the two wavelets to perform the inversion. The second step of the seismic inversion process is to estimate acoustic impedances. We used

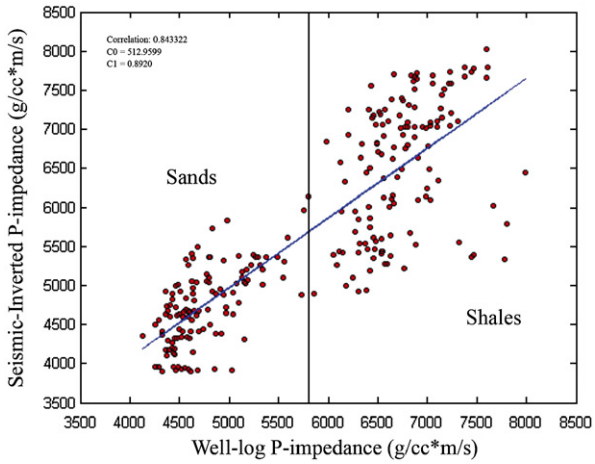

Fig. 4. Cross-plot of the pseudo acoustic impedance (P-impedance) logs extracted from the seismic-inverted acoustic impedance volume and the impedance logs derived from the sonic and bulk density logs in wells A10st and A8. Wells A10st and A8 are the only ones that include well- log measurements of both bulk density and P-wave velocity across the GNP2RB reservoir.

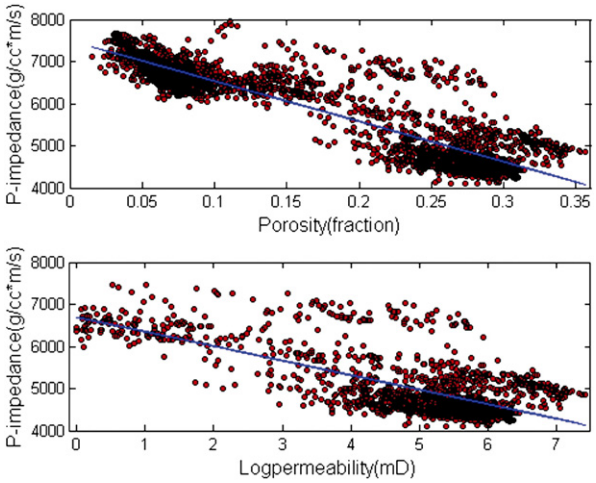

Fig. 6. Cross-plot of acoustic impedance and porosity and logarithm of permeability. Upper panel: Cross-plot of acoustic impedance and porosity values calculated with well-log data from wells A10st and A8. The blue line in the figure was constructed with linear regression analysis (correlation coefficient R^2 equal to −0.95). Lower panel: cross-plot of acoustic impedance and logarithm of permeability values calculated with well-log data from wells A10st and A8. The blue line in the figure was constructed with linear regression analysis (correlation coefficient, R^2 equal to 0.92).

the algorithm due to Debeye and Van Riel (1990), referred to as Constrained Sparse–Spike Inversion (CSSI), to invert acoustic impedances from post-stack seismic amplitude data. Rather than solving directly for reflectivity coefficients, Debeye and Van Riel (1990) pose the inverse problem to yield band-limited acoustic impedances subject to time-dependent value-range constraints.

A specific problem arises in the inversion of seismic amplitudes into acoustic impedance: the lack of low frequency components in both the post-stack seismic amplitude data and the reflectivity function. Because of this, the inverted acoustic impedances do not exhibit a low- frequency component, or trend of compaction (the drift typically seen in P-wave velocity logs with increasing depth due to mechanical compaction). The only way to include the compaction trend in the inverted band-limited acoustic impedances is to interpolate it from the compaction trend measured along existing wells (Grijalba-Cuenca et al., 2000). Addition of the compaction trend to inverted band-limited acoustic impedances yields the so-called inverted total acoustic impedances. The latter can be thought of as a smooth version of the wireline acoustic impedance log that would otherwise be acquired in a vertical well drilled at a given trace location in the seismic cube (Grijalba-Cuenca et al., 2000).

Fig. 4 is a cross-plot of the pseudo-impedance logs extracted from the cube of seismic- inverted acoustic impedances along well trajectories and the actual acoustic impedance log measured in the same wells. Well-log data included in this cross-plot were converted from depth to seismic-travel time, then low-pass filtered for alias protection and resampled to 4 ms in order to be compatible with seismic-inverted acoustic impedances (the same strategy is used in the rest of the paper when comparing well-log and seismic-derived properties). The correlation coefficient for the data on the cross-plot is 0.84. Such a relatively high correlation between the inverted and actual impedance well logs confirms that seismic amplitudes are reliable to estimate inter-well acoustic impedance. The time window for inversion was constrained by seismic horizons that defined the upper and lower boundaries of the GNP2RB reservoir. Those horizons also defined the lithological changes between sands and shales observed in Fig. 4. It now remains to ascertain whether acoustic impedance correlates with petrophysical properties.

Fig. 5 is a 3D rendering of the area of study showing existing well trajectories superimposed on a seismic-inverted acoustic impedance time horizon computed from the RMS value of acoustic impedance across the GNP2RB reservoir. In the figure, the areal extent of the reservoir is enclosed by structural faults as well as by stratigraphic boundaries; reservoir units coincide with anomalies of low acoustic impedance.

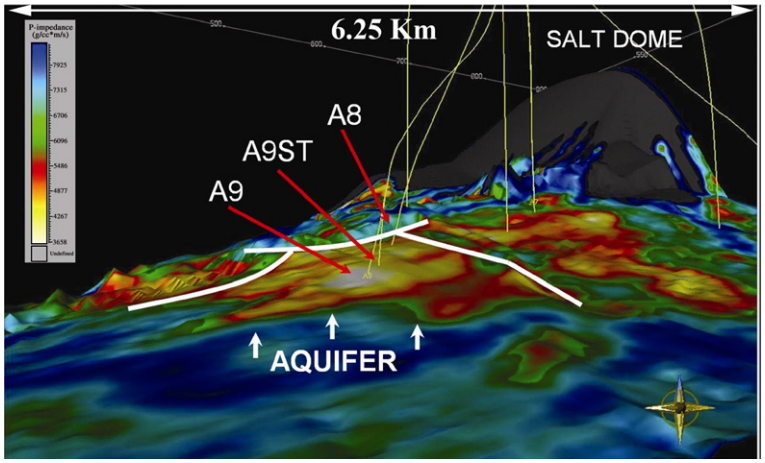

Fig. 5. 3D rendering of the area of study showing existing well trajectories superimposed on a seismic-inverted acoustic impedance time horizon computed from the RMS value of acoustic impedance across the GNP2RB reservoir. Low values of acoustic impedance are shown in yellow and high values in blue. In the figure, the areal extent of the reservoir is enclosed by structural faults as well as by stratigraphic boundaries; reservoir units coincide with anomalies of low acoustic impedance.

We note that amplitude-vs.-offset (AVO) effects could be present in the post-stack seismic amplitude data and that these effects may cause abnormal inversion results. In the absence of pre-stack seismic amplitude data and shear logs across the GNP2RB reservoir, we opted to perform blind-well tests to avert potential AVO effects on the inversion of post-stack seismic amplitude data. Comparison between acoustic impedance well logs and inverted impedances along the trajectories of blind wells did not indicate presence of artifacts in the inversion results due to unaccounted AVO effects.

In order to perform simulations of fluid production with time, it is necessary to construct cellular models where values of porosity and permeability are assigned to every simulation cell. We now proceed to explore whether these two inter-well petrophysical properties can be estimated from seismic-inverted acoustic impedances.

Fig. 6 shows cross-plots constructed to assess whether a statistical correlation exists between acoustic impedance and porosity (upper panel) and acoustic impedance and permeability (lower panel). Good quality sands exhibit low values of acoustic impedance (i.e. 4267–6096 g/cc*m/s) while poor quality sands and shales exhibit high values of acoustic impedance. The correlation coefficient was approximately −0.95 and −0.91 for acoustic impedance vs. porosity, and acoustic impedance vs. logarithm of permeability, respectively. Such relatively high correlations confirm that seismic-inverted acoustic impedance can be used to interpolate porosity and permeability in the inter-well region. We note that the trend between acoustic impedance and porosity is slightly different for the shale group than the one estimated in Fig. 6 due to mechanical compaction effects. However, we do not pursue a specific (and more accurate) correlation for shales given that the latter are regarded as impermeable in the simulations of fluid production subsequently described in this paper.

Fig. 7 is a cross-plot of acoustic impedance and calculated water saturation. Again, the GNP2RB reservoir sands are associated with low values of acoustic impedance. The cross-plot indicates that acoustic impedance alone cannot discriminate between the different saturating fluids involved (volatile oil, condensate gas, and water). No clear statistical correlation exists between water saturation and acoustic impedance. Only at the lowest range of the water saturation scale does acoustic impedance exhibit a small decrease below the otherwise flat trend. Castagna and Backus (1993) emphasized that, for the case of gas-water mixtures, the introduction of a minor amount of gas in the mixture causes a large decrease in the P-wave velocity. Presence of light oils (i.e. volatile oils) causes a further decrease of the P-wave velocity. Therefore, when these two fluids are present in the rock (condensate gas and volatile oil, as in the case of GNP2RB reservoir sands), the P-wave velocity will decrease with a decrease of water saturation regardless of their relative proportions in the total pore-volume saturation. The latter observation confirms that, for the case under consideration, acoustic impedance strongly correlates with porosity and weakly correlates with water saturation.

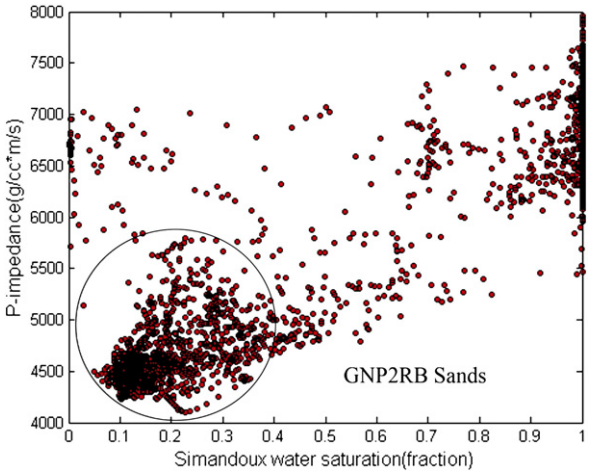

Fig. 7. Cross-plot of acoustic impedance and Simandoux water saturation constructed with well-log data acquired in wells A10st and A8. Well-log measurements acquired in the GNP2RB reservoir are enclosed by the black circle.

4. Geostatistics for seismic amplitude data integration

Geostatistical estimation techniques make use of histograms and spatial variograms (or auto-correlations functions) to describe the spatial continuity and smoothness of reservoir parameters away from existing measurement locations. Fig. 8 describes the spatial continuity model (semi-variogram) used in this paper to interpolate acoustic impedance.

Because seismic data involve horizontally dense measurements across the reservoir, we estimated the range of the horizontal semi-variograms (separately for the in-line and cross-line directions) from seismic-inverted acoustic impedances. This estimation was performed by honoring the embedding geometry and the proportional sedimentary layering defined by the two seismic horizons that mark the upper and lower boundaries of the GNP2RB reservoir. On the other hand, due to the high vertical resolution of well logs, we estimated the vertical range of the semi-variogram from acoustic impedance well logs. Fig. 8 also shows the normalized histogram constructed with the complete set of available measurements of acoustic impedance. This normalized histogram exhibits a bimodal distribution corresponding to the two main lithology types (sands and shales).

To understand the contribution of post-stack seismic amplitude data in the construction of static reservoir models, and to analyze potential difficulties and limitations of different geostatistical methods used to construct static reservoir models, in this paper we consider the following classes of constructed reservoir models:

1. Reservoir models constructed with the use of two standard geostatistical techniques, namely,
   (a) sequential Gaussian simulation of well-logs, and
   (b) collocated sequential Gaussian co-simulation of well-logs and seismic-inverted acoustic impedances.
2. Reservoir models constructed with a geostatistical inversion technique that simultaneously honors both seismic amplitude data and well logs.

Deutsch and Journel (1998) suggest that Sequential Gaussian Simulation (SGS) is probably the most flexible technique used to model reservoir heterogeneity and to quantify uncertainty. We implemented this procedure to construct stochastic realizations of reservoir porosity and permeability constrained by lithology. Fig. 9 shows that the distributions of porosity and logarithm of permeability sampled from well logs exhibit a bimodal statistical behavior due to the existence of two main lithologies: sands and shales. To honor these distributions, we populated inter-well porosity and logarithm of permeability in the GNP2RB reservoir following two sequential steps: (a) geostatistical simulation of the facies (two possible outcomes: sands and shales) and (b) Gaussian simulation of porosity and logarithm of permeability within each of the simulated facies.

The geostatistical simulation of the two facies is based on synthetic litho-type logs. The latter are constructed from the shale-volume log by imposing a cut-off that discriminates between sand and shales (i.e. 0.45). Normalized histograms used to estimate the global probability of occurrence, p, of the two facies, indicated values of 58% for sands and 42% for shales, respectively. Subsequently, the selection of a litho-type for each cell in the geostatistical grid was performed using litho-type dependent semi-variograms, where the corresponding sill (0.25) was estimated from the relationship (Lortzer and Berkhout, 1992)

$$\text{sill} = p(1-p). \tag{2}$$

For the case of Gaussian collocated co-simulation (CSGS), seismic-inverted acoustic impedances constitute a secondary input that remains

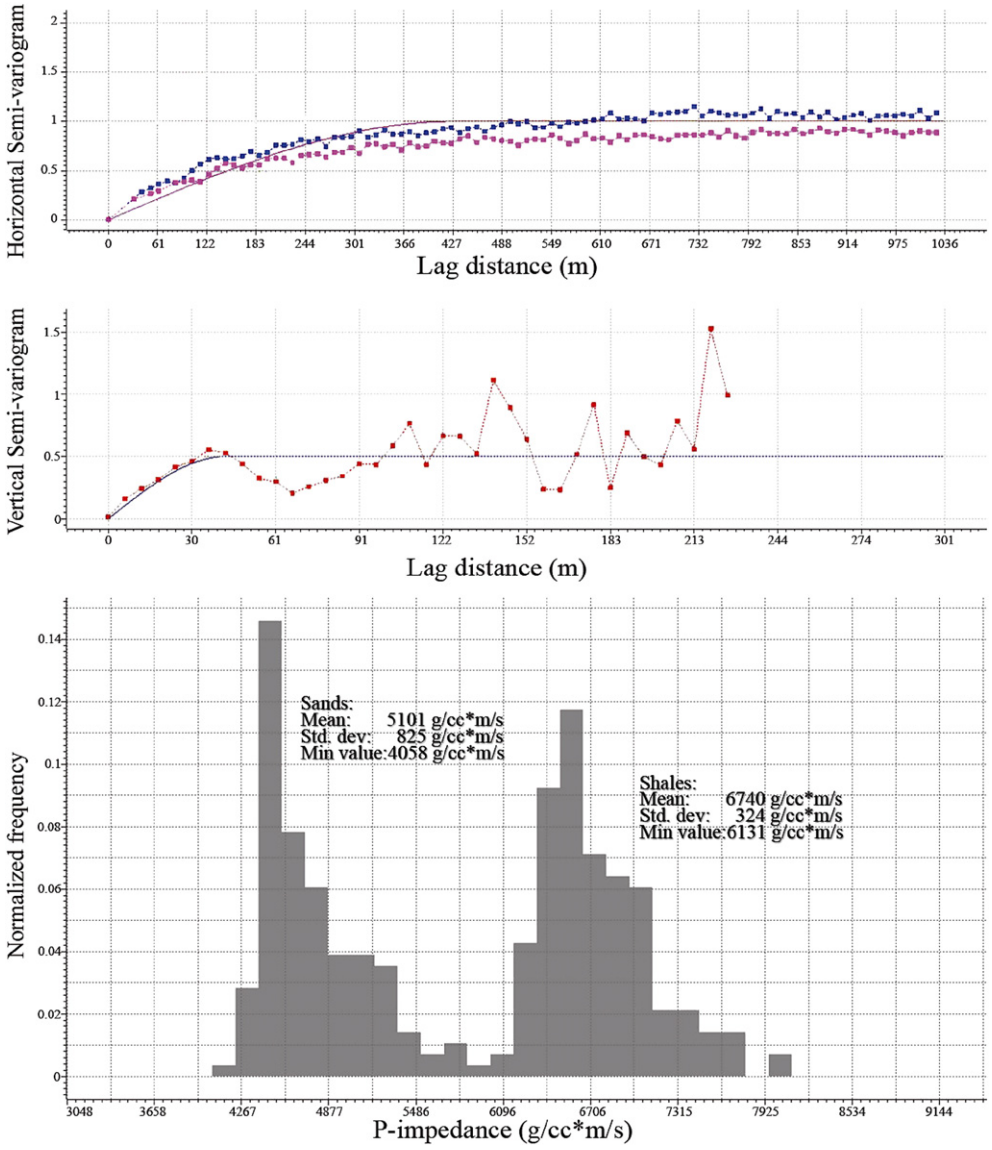

Fig. 8. Spatial continuity model (semi-variogram) used to populate acoustic impedance in the inter-well region of the GNP2RB reservoir. Top panel: sampled (discrete points) and modeled (continuous lines) horizontal semi-variograms for the in-line and cross-line seismic directions. Semi-variograms were approximated with a spherical model of range and sill equal to 427 m and 1, respectively. Mid Panel: sampled (discrete points) and modeled (continuous line) vertical semi- variograms. Well-log acoustic impedances were used to construct the sampled vertical semi-variogram, whereas the modeled vertical semi-variogram was constructed using a spherical model of range and sill equal to 427 m and 0.5, respectively. Lower panel: normalized histogram constructed with well-log acoustic impedances.

statistically correlated to both porosity and logarithm of permeability (Fig. 6). Accordingly, the Gaussian simulations of porosity and permeability were constrained by their local correlation with acoustic impedance.

Geostatistical inversion (GI) is a stochastic inversion procedure that honors the available seismic amplitude data, the well logs, and the assumed semi-variograms and probability density functions (PDFs). Seismic amplitude data are honored in an iterative manner. For the specific implementation of GI considered in this paper, porosity and logarithm of permeability are first populated in the reservoir using SGS. The populated values of porosity and logarithm of permeability are transformed to acoustic impedance using pre-defined statistical correlations[1]. The transformed value of acoustic impedance is then used to simulate the post-stack seismic amplitude data trace-by-trace via one-dimensional convolution. Subsequently, the global seismic misfit is calculated with the sum of squared differences between the simulated seismic amplitudes and the measured seismic amplitudes over the complete post-stack seismic cube. Minimization of the global seismic misfit is achieved in a monotonic fashion through a sequence of iterations. Each iteration consists of a random walk through the entire seismic cube. The random walk is performed in the 3D space defined by both seismic time and horizontal location. Simulations of both porosity and permeability are performed for the particular location designated by the random walk followed by the corresponding transformation to acoustic impedance and calculation of the global seismic misfit. Simulated annealing is used to decide whether to accept or reject the simulated acoustic impedance at a particular location in the seismic cube in view of: (a) the change in global seismic misfit due to that simulation and (b) the prescribed criterion for global misfit reduction from iteration to iteration. One iteration is deemed complete when simulations of porosity and logarithm of permeability have been accepted or rejected at all the nodes in the seismic cube (i.e. when the random walk has reached all points in the seismic cube, Grijalba-

[1] We note that, alternatively, the inversion procedure could be implemented by first simulating acoustic impedance and subsequently transforming the simulated value of acoustic impedance into values of porosity and logarithm of permeability using the same pre-defined statistical correlations. However, we favor the reverse approach because it enables a more efficient connection with lithology types (either sands or shales in this case) via sequential-indicator simulation.

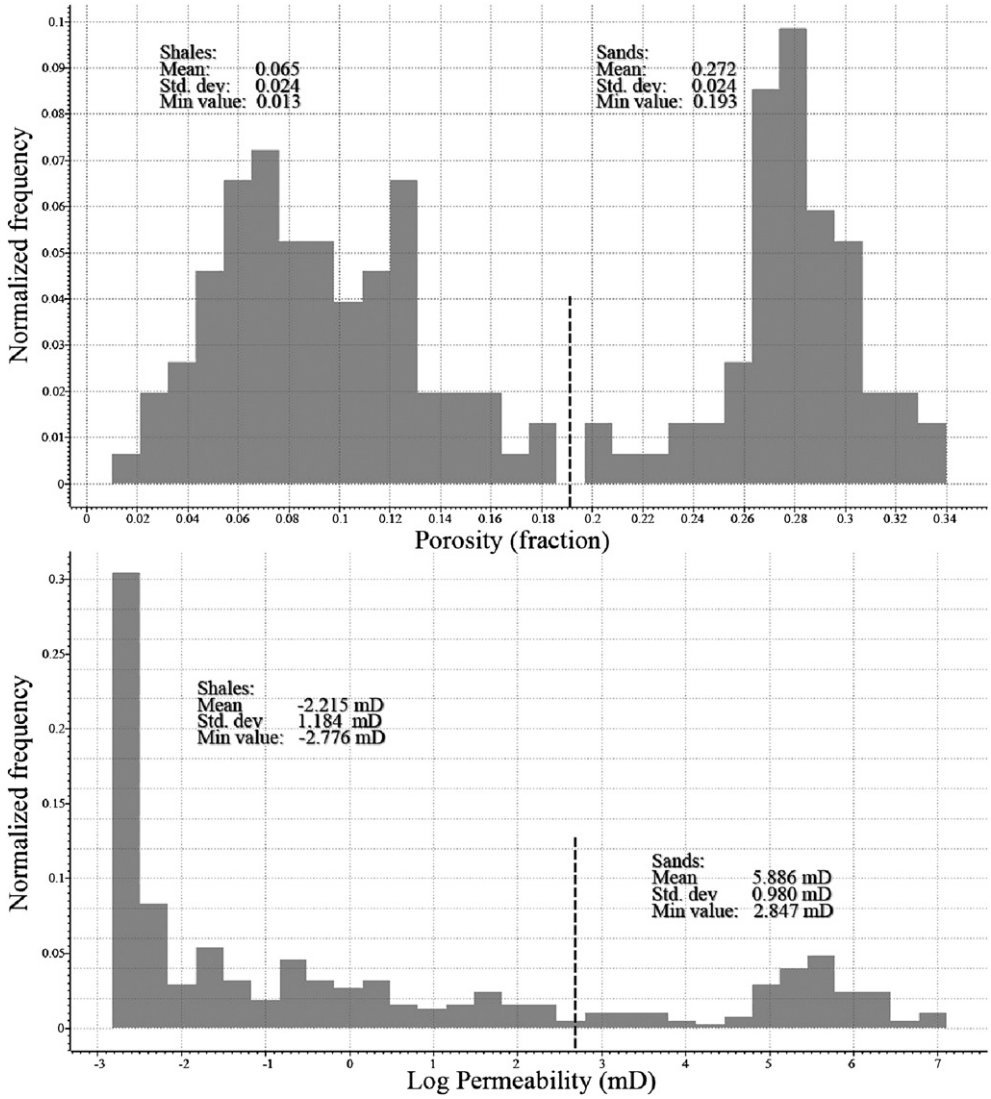

Fig. 9. Normalized histograms of porosity (upper panel) and logarithm of permeability (lower panel) constructed with well-log data acquired in wells A10st and A8 across the GNP2RB reservoir.

Cuenca et al., 2000). The inversion comes to an end when the global seismic misfit has decreased to a prescribed lower bound (usually determined by the signal-to-noise ratio inherent to the seismic amplitude data and possible AVO effects) or else when the number of iterations has reached a prescribed maximum. Independent inversions of porosity and permeability can be performed by starting the process over with independent initial realizations of porosity and permeability via SGS (iteration no. zero). An important feature of geostatistical inversion is that the vertical sampling interval of the inverted distributions can be adjusted anywhere between the vertical sampling interval of well logs and seismic amplitude data.

We performed 90 independent geostatistical inversions of acoustic impedance, porosity, and logarithm of permeability within the GNP2RB reservoir enforcing the same vertical sampling interval as that of the seismic data (4 ms). Each of the 90 geostatistical inversions was initialized with an independent random seed. Convergence of the geostatistical inversion algorithm required no more than 35 iterations for each of the random initial models. Fig. 10 shows plan views of the cross-correlation between the measured and the numerically simulated post-stack seismic amplitude data as a function of the number of iterations (minimum cross-correlation is zero and maximum cross-correlation is one). The first map (iteration zero) corresponds to the seismic cross-correlation associated with SGS (here used to initialize the inversion). Subsequent iterations entail a monotonic increase in the seismic cross-correlation. For the last iteration (iteration number 35), the cross-correlation has reached the final value of 0.95. This target correlation value is consistent with independent estimates of signal-to-noise ratio obtained with blind-well tests.

Unless otherwise noticed, construction of reservoir models with the SGS, CSGS, or GI techniques described in this paper made use of the same semi-variogram models (shown in Fig. 8) to populate reservoir porosity and logarithm of permeability between wells. Moreover, the simulations of porosity and logarithm of permeability were preceded by the simulation of lithology (two possible outcomes: sands or shales).

Spatial distributions of porosity and permeability rendered by SGS, CSGS, and GI were transformed from seismic time to depth using the available distribution of interval P-wave velocities. We generated a P-wave velocity cube from the interpolation of P-wave velocity logs, previously transformed from measured depth to true vertical depth (TVD). In addition, the conversion from seismic time to depth was guided by the two seismic horizons marking the lower and upper boundaries of the GNP2RB reservoir. The transformation enforced a uniform sampling interval equal to 10 m calculated with the average P-wave velocity of well-log measurements across the GNP2RB reservoir, and the time sampling interval of the seismic amplitude data. The

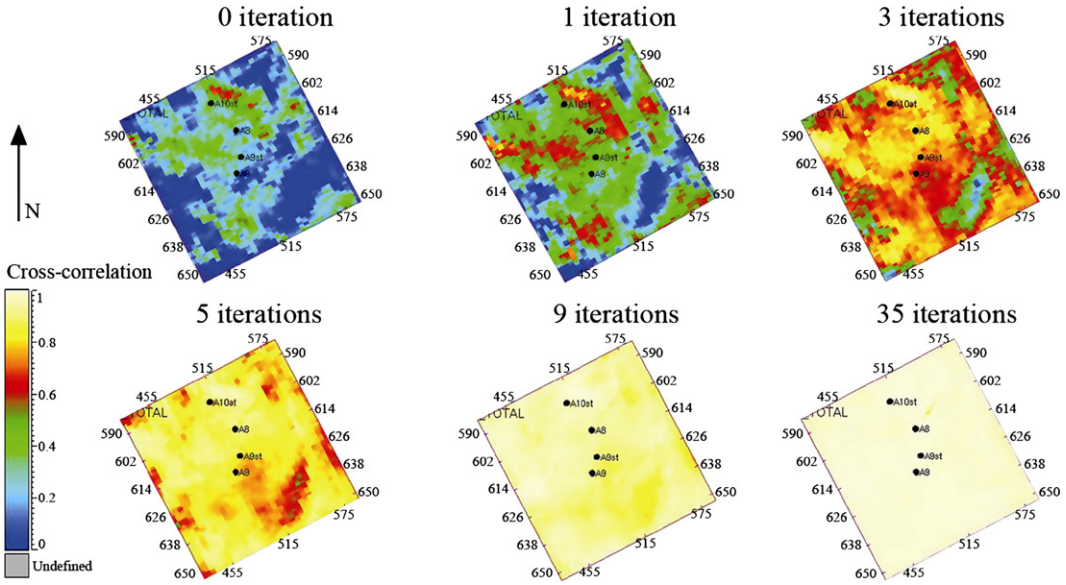

Fig. 10. Maps of the cross-correlation between measured and simulated post-stack seismic amplitude data as a function of the number of iterations in the geostatistical inversion of inter-well acoustic impedance. The maps show well locations in black and seismic correlation with color-coded values. Low values of seismic correlation are shown in dark blue and high values in yellow.

effect of depth sampling interval on the constructed reservoir model is considered in a subsequent section of this paper.

5. Reservoir and fluid description

The reservoir under study included a gas cap before the onset of production. Production commenced with an initial pressure close to the saturation or bubble-point pressure. The volatile nature of the oil present in the GNP2RB originated even more volatile components at the gas cap (condensates); hence, there is more than one single production mechanism during the pressure depletion life of the reservoir under study. The major production mechanism is water-drive by an external aquifer, although solution gas- or dissolved gas-drive and gas-cap expansion are also responsible for primary fluid production. To diagnose the existence of a water drive, the observation of monotonically increasing water production was not the only clue; we employed a combination of oil, water, and gas material balance equations to determine water influx and to confirm the mechanisms of primary fluid production and pressure depletion in the GNP2RB reservoir. This was accomplished with synthetic Pressure-Volume-Temperature (PVT) parameters generated with empirical correlations (Walsh and Lake, 2003). Table 1 is a summary of the PVT parameters employed to perform the material balance calculations. Also, Fig. 11 describes the results of the material balance calculations indicating the predominant production drive mechanisms and the calculated water influx. From production measurements, it was found that the gas cap contained condensates of approximately 50 API gravity; therefore, the volatilized oil-gas ratio was in the range of 0–292 m^3/MM m^3 (0–52 STB/MMscf). Fig. 12 shows the cumulative oil, gas, and water production for each well plus the time record of static reservoir pressure for the entire reservoir. From available geological information and fluid saturation inferred from well logs, it was found that the location of well A8 was up dip in the structure and close to the primary gas cap, while well A9ST was located down dip in the structure and close to the water-oil contact. Both wells were completed in the reservoir's oil leg where the gravity of the stock-tank oil was 40 API.

6. Numerical simulation of reservoir production

We simulated the dynamic behavior of reservoir GNP2RB as a modified black-oil tank model with an active aquifer recharge at the bottom and a gas cap at the top. The locations of the water-oil and gas-oil contact were defined from electrical resistivity, neutron porosity, and bulk density logs. Moreover, the reservoir was assumed to be in capillary equilibrium prior to fluid production.

Table 1
Summary of the fluid properties and Pressure-Volume-Temperature (PVT) parameters, rock-fluid properties, and spatial discretization associated with the hydrocarbon reservoir model considered in this paper

	Properties	Values and units
PVT fluid parameters	Reservoir pressure	24683 kPa
	Bubble pressure, Pb	24683 kPa
	R_{si}, standard conditions/ standard conditions	566 m^3/m^3
	R_{vi}, standard conditions/ standard conditions	292 m^3/MMm^3
	B_{oi}, reservoir conditions/ standard conditions	2.84 m^3/m^3
	B_{gi}, reservoir conditions/ standard conditions	3.20 m^3/Mm^3
	B_{wi}, reservoir conditions/ standard conditions	1.02 m^3/m^3
	Reservoir temperature	360.65°K
Fluids	Water density	1.1 g/cm^3
	Oil density	0.8251 g/cm^3
	Specific gas gravity	0.65
	Water viscosity	0.34E−03 Pa·s
	Oil viscosity	0.274E−03 Pa·s at 1379 kPa
	Gas viscosity	0.013E−03 Pa·s at 101 kPa
	Water compressibility	9.73E−10×1/Pa at 24683 kPa
	Oil compressibility	6.41E−09×1/Pa at 24683 kPa
	Gas compressibility	4.04E−08×1/Pa at 24683 kPa
Rock-fluid properties	Irreducible water saturation	12%
	Residual oil saturation	10%
	Average effective porosity	27%
	Average permeability	354 mD
	Formation compressibility	2.34E−11×1/Pa
	Relative permeability water end-point	0.3
	Relative permeability oil end-point	0.8
	Relative permeability gas end-point	0.9
	Vertical to horizontal permeability ratio	1.0
	Location of pressure datum	2943 m (below the sea bottom)
	Location of gas-oil contact	2867 m (below the sea bottom)
	Location of water-oil contact	2957 m (below the sea bottom)
Simulation	Number of cells (x,y,z)	15×36×15
	Cell size (dz,dy,dz)	25 m×12 m×10 m

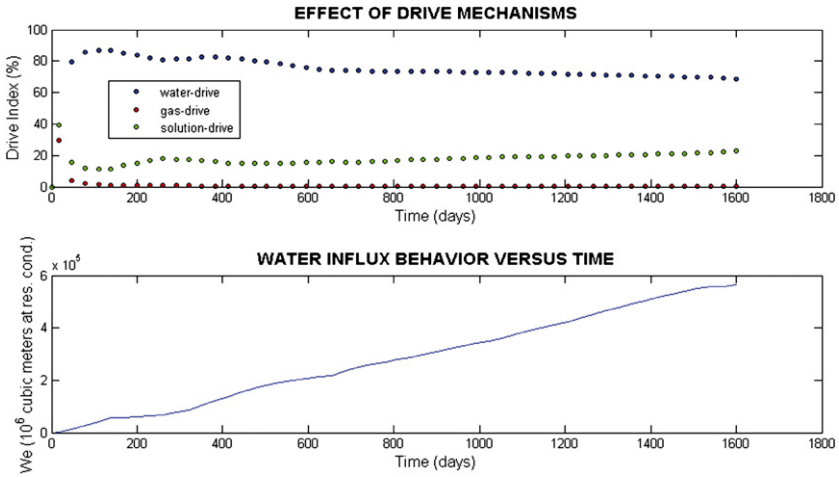

Fig. 11. Material balance calculations. Top panel: estimated drive indexes governing fluid production in the GNP2RB reservoir. Bottom panel: calculated cumulative water influx versus time after the onset of production.

The number of grid cells used to simulate primary fluid recovery was the same as those used to simulate the post-stack seismic amplitude data. Upscaling was not performed on the property cells. The number of reservoir simulation cells in the x and y directions coincided with the number of seismic in-lines and cross-lines, respectively. In the z-direction, the number of reservoir simulation cells was made consistent with the vertical sampling interval of the seismic amplitude data transformed to depth, i.e. 10 m. Table 1 describes the fluid properties, rock-fluid properties, and spatial discretization associated with the hydrocarbon reservoir model considered in this paper.

We constructed the final reservoir models with (a) a corner-point fluid-flow grid of cell dimensions equal to 25×12×10 m in the x, y, and z directions, respectively, (b) 15×36×15 grid cells in the x, y, and z directions, respectively (8100 reservoir cells), (c) a closed reservoir with active aquifer recharge, and (d) two producing wells. Thirty independent stochastic realizations of porosity and permeability were calculated for each of the three geostatistical techniques used to populate the inter-well region of the reservoir. The realizations were input separately to the multi-phase black-oil simulator ECLIPSE™. Brooks-Corey type relative permeability and capillary pressure curves (Brooks and Corey, 1966) were used in the multi-phase fluid flow simulation.

In this field study, 1599 days (approximately 4 years) of production history were available. Oil flow rates in each well were specified in the simulations, with water and gas production rates, as well as pressure depletion used to assess the agreement between the simulated and the measured time records of fluid production. Because the principal fluid production mechanism was water-drive, we used plots of cumulative water production in the reservoir to quantify the impact of the constructed spatial distributions of porosity and permeability on the simulated time records of fluid production.

Fig. 13 compares the cumulative water production versus time for the three different statistical techniques (SGS, CSGS, and GI) used to populate porosity and permeability in the GNP2RB reservoir. Results

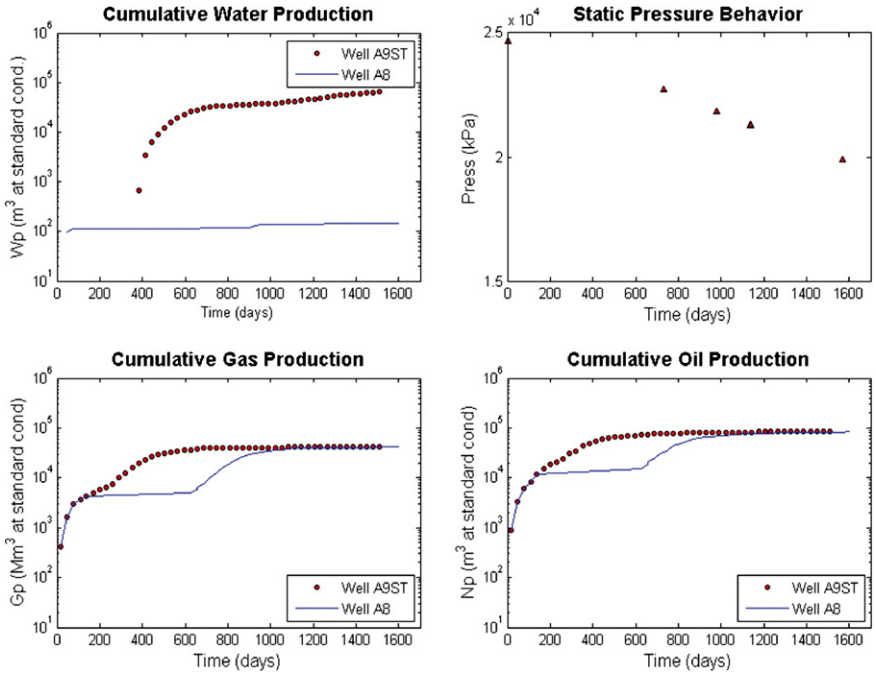

Fig. 12. Plots of the time evolution of cumulative fluid production and reservoir pressure in the GNP2RB reservoir after the onset of production for wells A9ST and A8.

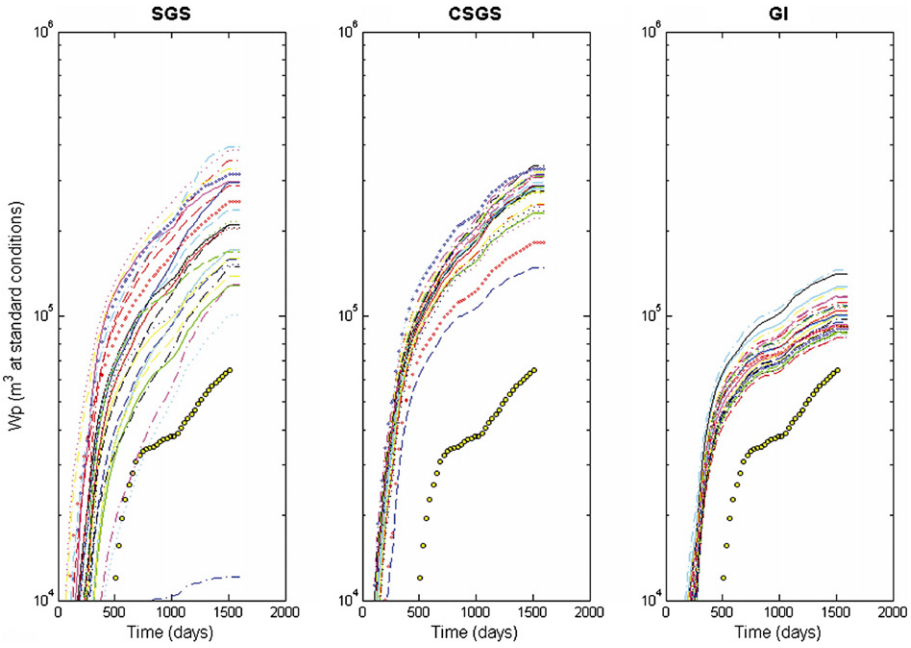

Fig. 13. Comparison of the time evolution of measured and numerically simulated cumulative water production after the onset of production. Actual measurements of water production are identified with yellow dots. Each panel describes the cumulative water production numerically simulated for 30 independent stochastic realizations of porosity and permeability in the GNP2RB reservoir using sequential Gaussian simulation (SGS), collocated co-simulated sequential Gaussian simulation (CSGS), and geostatistical inversion (GI).

obtained from 30 independent models for each case were compared against the measured time records of water production (the latter are identified with yellow dots in Fig. 13). Sequential Gaussian simulation consistently yielded the highest value of cumulative water production as well as the largest spread among the simulations. For the collocated Gaussian co-simulation case, both the spread and the magnitude of the simulations decreased compared to those of SGS. Therefore, we conclude that the reliability of the constructed reservoir models improves with the use of seismic amplitude data. Geostatistical inversion yielded the least biased and most accurate simulations of fluid production. Models generated with the use of seismic amplitude data produced the best agreement with the measured time records of fluid production and exhibited the smallest spread among all the simulation results. Moreover, we found a good agreement between simulated and measured time records of both cumulative gas production and reservoir pressure.

The upper panel in Fig. 14 shows a seismic-depth cross-section of one porosity realization obtained separately with the three geostatistical simulation procedures considered in this paper (SGS, CSGS, and GI). Different connectivity patterns of reservoir porosity are associated with each case, thereby explaining why the corresponding simulations of time records of fluid production were so drastically different for each method used to populate reservoir porosity and permeability. In this case, geostatistical inversion yields the spatially smoothest rendering of porosity because of the direct enforcement of the constraint to honor seismic amplitude variations. The same remark applies to the case of permeability described in the lower panel of Fig. 14.

7. Uncertainty analysis and variability of dynamic behavior

The objective of this paper is to assess data sensitivity and uncertainty in the construction of static spatial distributions of porosity and permeability in the GNP2RB reservoir. To appraise reservoir models constructed with geostatistical inversion and conventional geostatistical simulation techniques, we performed 90 conditional fluid-flow simulations (Base Cases; refer to Table 2). The approach described in this paper is a step forward toward establishing a systematic procedure to assess non-uniqueness in the predictions of time records of fluid production and reservoir pressure depletion.

It has been recognized that history matching is not only a computationally challenging problem to solve but is also riddled with non-uniqueness. Non-uniqueness means that there are multiple realizations of model parameters that honor the measured time records of fluid production (Landa and Guyaguler, 2003). Therefore, it is not only desirable to estimate reservoir models that entail an acceptable agreement with the measured time records of fluid production but also to quantify their corresponding non-uniqueness (or uncertainty).

Figs. 15–17 show Box plots (Box et al., 1994) of normalized cumulative water production constructed with the simulated time record of fluid production for 90 independent realizations of porosity and permeability. In a Box plot (Box et al., 1994), the variability of a prediction is measured by the size of the vertical boxes. Biases are detected when the median value significantly departs from the true value, or when the length of the box does not include the truth case (Varela et al., 2002).

Fig. 15 summarizes the sensitivity analyses performed for the base cases described in Table 2. We measure the variability of the simulations of dynamic fluid production by making perturbations to the spatial distributions of porosity and permeability. In that figure, base cases describe the normalized cumulative water production simulated with 90 independent reservoir models constructed with SGS, CSGS, and GI.

We note that the time records simulated with SGS reservoir models, generated through the interpolation of well logs, do not agree with the actual measurements. Reservoir models constructed with co-simulation entail considerably less spread in the corresponding time records of fluid production than reservoir models constructed with SGS. This exercise indicates that the use of seismic amplitude data has a positive impact on the constructed reservoir models.

However, geostatistical inversion provided the most accurate and least biased simulations of production measurements including cumulative gas production and pressure depletion.

We carried seven sensitivity analyses to further appraise the accuracy and reliability of reservoir models constructed with geostatistical inversion. Table 2 summarizes the various exercises of sensitivity

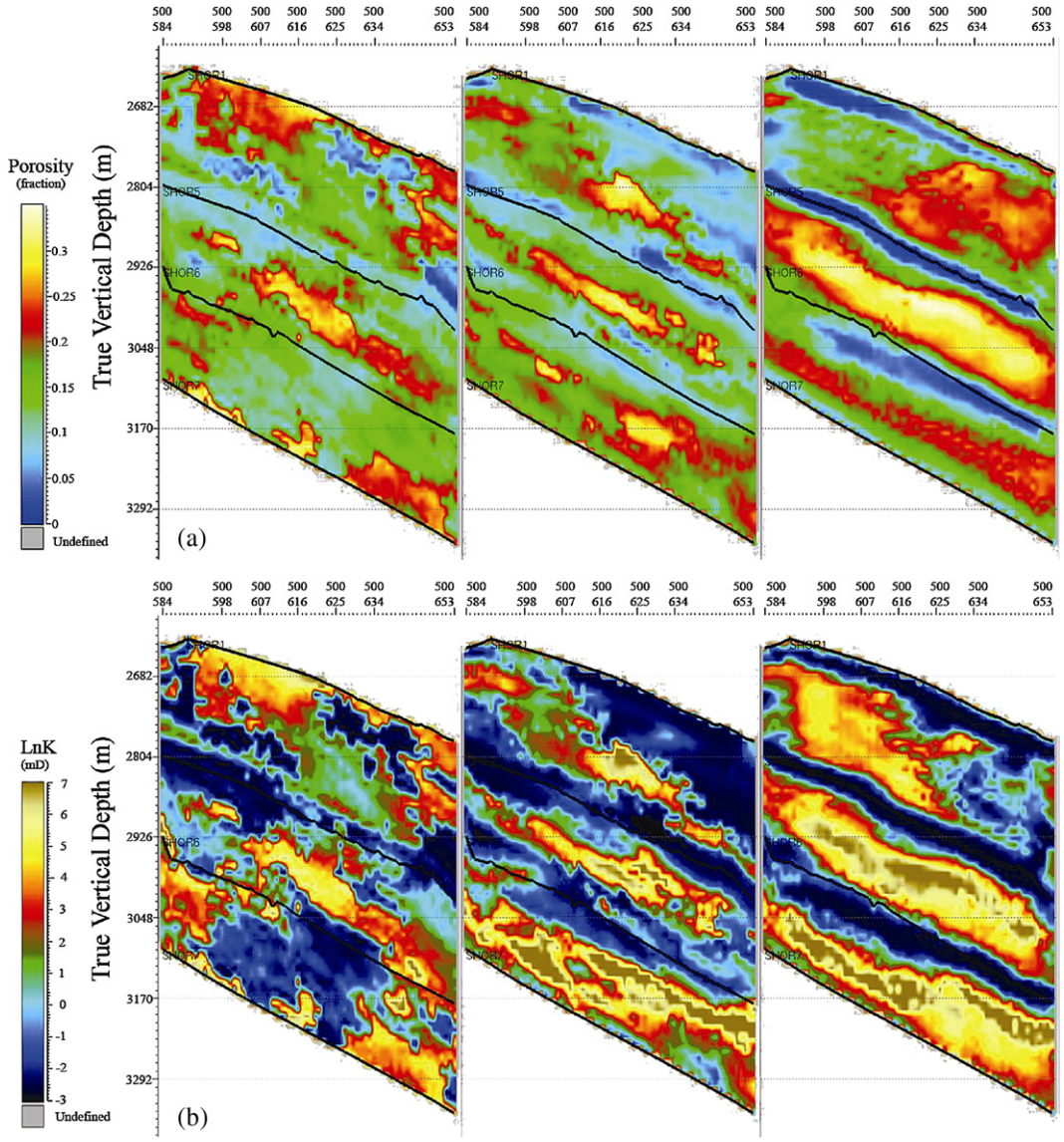

Fig. 14. Cross-sections of one spatial realization of inter-well porosity and one realization of logarithm of permeability obtained with three different geostatistical techniques with a vertical sampling interval of 4 ms. Panel (a) shows low values of porosity in blue and high values in yellow. From left to right, the figure shows inter-well porosity distributions rendered by sequential Gaussian simulation, collocated co-simulated sequential Gaussian simulation, and geostatistical inversion. Panel (b) shows low values of logarithm of permeability in dark blue and high values in yellow. From left to right, the figure also shows inter-well logarithm of permeability distributions rendered by sequential Gaussian simulation, collocated co-simulated sequential Gaussian simulation, and geostatistical inversion.

analysis designed to appraise various forms of spatial variability in the porosity and permeability models, whereas Table 3 summarizes the exercises of sensitivity analysis designed to assess various forms of perturbations of rock-fluid properties.

Several rock-fluid parameters can have a substantial impact on the dynamic behavior of the reservoir. However, given that the main fluid production mechanism in the GNP2RB reservoir is water-drive, for the corresponding sensitivity analysis we chose to focus our attention on perturbations of both the end-point of water relative permeability and the imbibition water-oil capillary pressure curves.

In Fig. 16, Sensitivity Analysis No. 1 indicates that the most reliable simulations of time records of fluid production are associated with geostatistically inverted reservoir models. Often, standard geostatistical simulation procedures remain highly sensitive to both the assumed semi-variogram model (and parameters thereof) and to the relative location and number of available wells. By contrast, geostatistical inversion relies heavily on the seismic amplitude variations between wells and as such, is less sensitive to the choice of semi-variogram model and related parameters as well as to the number and location of the input wells. We used spherical semi-variograms to model the spatial variability of porosity and logarithm of permeability, and adjusted the corresponding sills to a normalized value of 0.5 for each litho-type (sands and shales). Moreover, Sensitivity Analysis No. 1 was performed by changing the lateral range of the semi-variograms from 427 m to 229 m. Gambús (2005) described the impact of changing the range of the lateral semi-variogram on the spatial distributions of porosity constructed with two different geostatistical techniques (CSGS and GI). Results indicated that spatial distributions constructed with GI were less sensitive to the choice of semi-variogram model than spatial distributions constructed with CSGS.

Gambús and Torres-Verdín (2002) showed that geostatistical inversion could be used to adjust the vertical resolution of the simulated reservoir models anywhere between the vertical resolutions of well logs and seismic amplitude data. Sensitivity analysis No. 2 in

Table 2
Summary of the nomenclature used to identify the numerical experiments conducted in this paper to study the sensitivity of the time records of fluid production measurements to spatial variations of porosity and permeability

Sensitivity analysis	Case	Sequential Gaussian simulation of well −logs	Collocated co-simulated sequential Gaussian simulation of well −logs and AI	Geostatistical Inversion: well −logs+AI+seismic data
Key control	Base Cases	SGS	CSGS	GI
Sensitivity analysis number 1: lateral range of the variogram	Rx=427 m	SGS	C-1	GI-1
	Rx=229 m		C-2	GI-2
Sensitivity analysis number 2: seismic time sampling interval	$\Delta t_{=4\ ms}$			GI-1
	$\Delta t_{=2\ ms}$			GI-3
	$\Delta t_{=1\ ms}$			GI-4
Sensitivity analysis number 3: $\phi-k$ correlation (50% — perturbation trend)	γ=1; α=7.68; β=7.24			GI-1
	γ=1; α=3.84; β=3.62			GI-5
Sensitivity analysis number 4: error in the correlation $\phi-$AI (3% — perturbation trend)	R^2=−0.95			GI-1
	R^2=−0.92			GI-6
Error in the correlation $k-AI$ (9% — perturbation trend)	R^2=−0.91			GI-1
	R^2=−0.84			GI-7
Error in the correlations ϕ, $k-$AI	Combination of GI-6, and GI-7			GI-8
Sensitivity analysis number 5: vertical to horizontal permeability ratio (K_V/K_H)	K_V/K_H=1			GI-1
	K_V/K_H=0.5			GI-9
	K_V/K_H=0.1			GI-10
Sensitivity analysis number 6: wavelets	Wavelet number 1			GI-1
	Wavelet number 2			GI-11

Fig. 16 shows Box plots of normalized cumulative water production for reservoir models constructed with vertical sampling intervals of 4 ms (time sampling interval of the seismic amplitude data), 2 ms, and 1 ms. Results indicate that the spread and bias of the simulated time records of water production remain relatively unaffected by the choice of vertical sampling interval. A slight, albeit inconclusive bias in the time records of fluid production ensues when increasing the vertical sampling interval of the realizations of porosity and permeability.

For Sensitivity Analysis No. 3, the intention was to explore the variability of the simulated time records of fluid production due to a perturbation in the assumed porosity-permeability correlation. Such an exercise was also intended to assess whether an erroneous porosity- permeability correlation could significantly affect the simulated time record of fluid production, especially when compared to the corresponding variability of fluid production due to spatial variability of porosity and permeability. To this end, we enforced a 50% perturbation in the porosity-logarithm of permeability rock-core trend shown in Fig. 3. Results from this exercise indicate that permeability has a strong impact on fluid production; small values of permeability not only reduce the uncertainty but also increase the bias of the simulated time records of fluid production.

Sensitivity Analysis No. 4, also described in Fig. 16, summarizes the results of exercises performed to assess the influence of errors in (a) the assumed porosity-acoustic impedance correlation, (b) the assumed permeability-acoustic impedance correlation, or (c) both of them. As indicated in Fig. 16, the largest variation on the simulated time record of fluid production was obtained for the case of a perturbation in the permeability-acoustic impedance correlation (refer to Table 2 for a definition of the cases).

Results from Sensitivity Analysis No. 5 are described in Fig. 16. This is an exercise intended to quantify the influence of variations of permeability anisotropy on the simulated time records of fluid production and pressure depletion. To this end, we considered values of 1, 0.5, and 0.1 for the assumed ratio between vertical and horizontal permeability (K_V/K_H). Simulations indicated that permeability anisotropy had a significant influence on the time records of fluid production. A 50% reduction in the value of vertical permeability entailed a sizable spread in the simulated time records of fluid production. Moreover, when the vertical permeability decreased to 90% of its original value the simulated time records of fluid production exhibited a considerable bias.

Sensitivity Analysis No. 6 is intended to quantify the influence of the estimated seismic wavelet on the simulated time records of fluid production. Results form this exercise are described in Fig. 16. The perturbation of wavelet properties for this exercise consisted of a 45°-phase variation of the original wavelet. This exercise indicated that perturbations in the assumed wavelet increased the bias of the predicted time records of cumulative water production. Phase variations smaller than 10° did no appreciable change in the simulated time records of fluid production and pressure depletion.

From the results described above, it follows that the combined use of seismic amplitude data, well logs, and rock-core measurements drastically reduced the uncertainty and the bias of the simulated time records of fluid production and pressure depletion. However, we observed significant biases in the simulations of cumulative water production when making perturbations to the spatial distributions of porosity and permeability (Table 2; Fig. 16). Our study suggests that special attention and care must be exercised when (a) estimating permeability and establishing a relationship between porosity and acoustic impedance, (b) choosing the value of vertical to horizontal permeability ratio (anisotropy), and (c) estimating the wavelet from seismic- amplitude data and well logs.

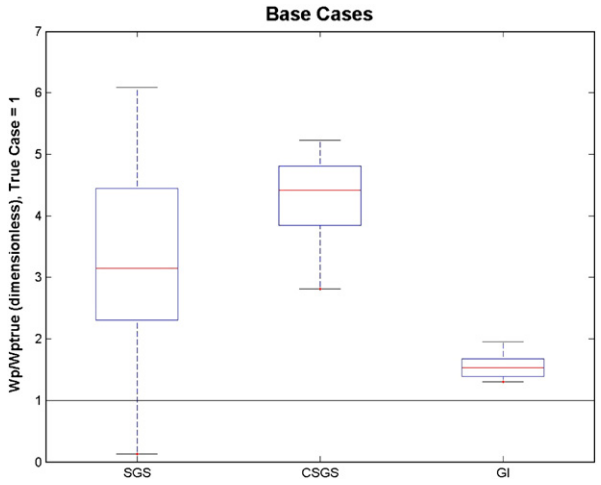

Fig. 15. Box plots of normalized cumulative water production for the base cases described in Table 2. The plots were constructed with numerical simulations of water production for 30 independent realizations of inter-well porosity and permeability rendered by 3 geostatistical techniques.

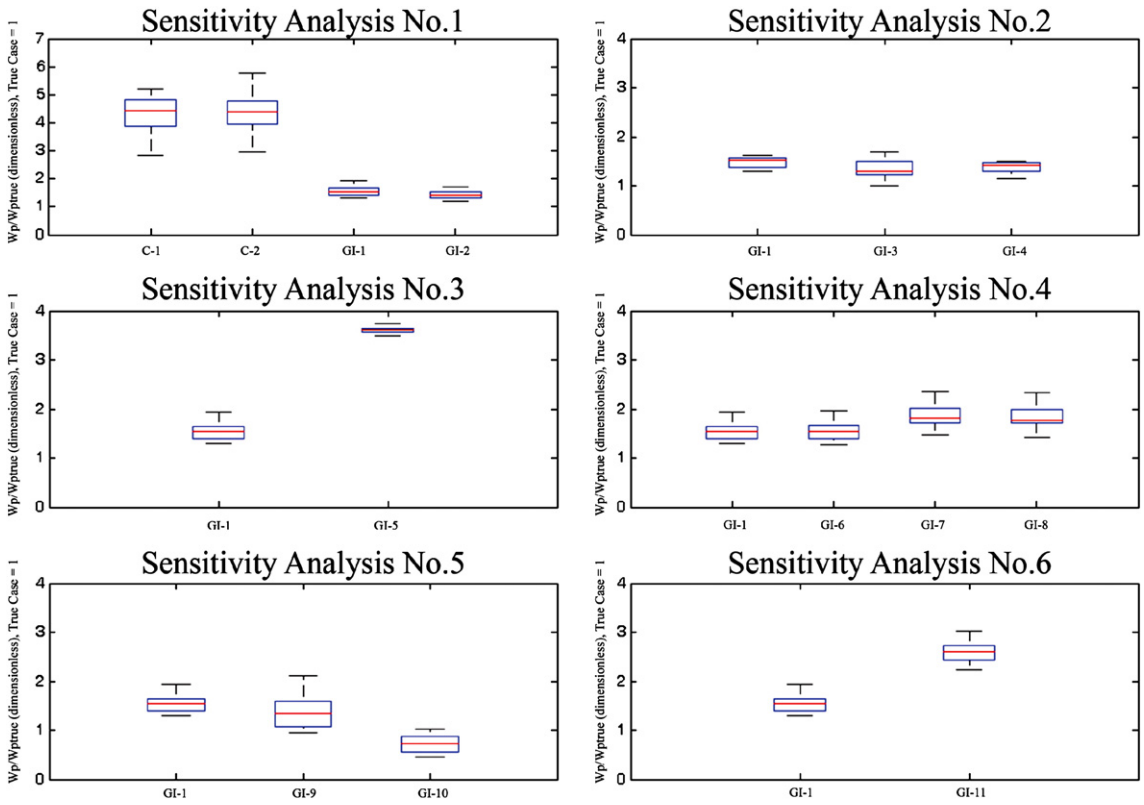

Fig. 16. Box plots of normalized cumulative water production for various cases of sensitivity analysis. Box plots were constructed using numerical simulations of water production for 30 independent realizations of inter-well porosity and permeability. See Table 2 for a definition of the cases. The actual measurement of total cumulative water production is identified with the horizontal black lines (Wp = 1.0).

Varela et al. (2002) stated that biased predictions of fluid recovery could be associated with pure fluid-flow phenomena to which post-stack seismic data remain insensitive. Therefore, we considered perturbations of the fluid and rock-fluid properties (i.e. end-point water relative permeability, and the water-oil imbibition capillary pressure curve) to assess the influence of these parameters on the reliability and accuracy of the predictions of fluid production.

Sensitivity Analysis No. 7, described in Fig. 17, is intended to assess the effect of a perturbation of the fluid and rock-fluid properties on the simulated time records of fluid production. Comparison of the latter results against those of the previous cases indicates that the associated spread and bias of the predictions are not significant.

In summary, the results described in this paper consistently indicate that, for the reservoir under consideration, spatial variations of porosity and permeability remain the primary controls of the time behavior of fluid production and pressure depletion. This conclusion cannot be generalized to the analysis of other types of hydrocarbon reservoirs. However, the systematic methodology described in this paper can still be used to assess the influence of a variety of

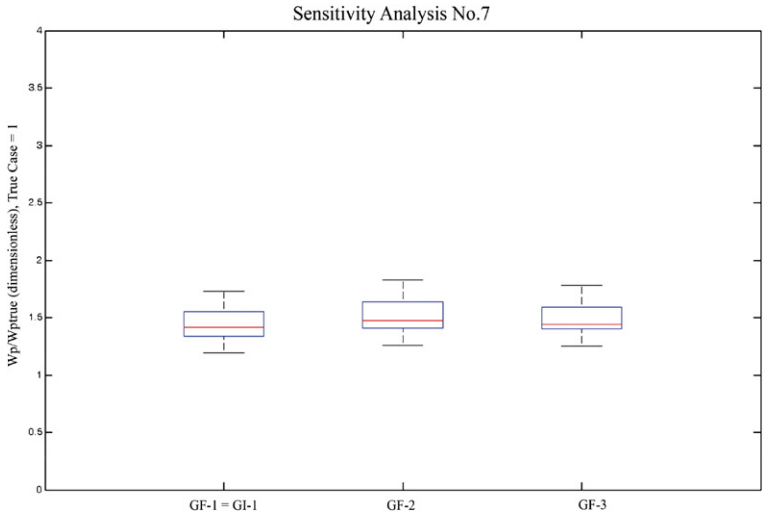

Fig. 17. Box plots of normalized cumulative water production for various cases of sensitivity analysis. Box plots were constructed using numerical simulations of water production for 30 independent realizations of inter-well porosity and permeability. See Table 3 for a definition of the cases. The actual measurement of total cumulative water production is identified with the horizontal black lines (Wp = 1.0).

Table 3
Summary of the nomenclature used in this paper to identify the numerical experiments conducted to assess the sensitivity of the time records of fluid production measurements to fluid and rock-fluid properties

Sensitivity analysis number 7	Case	Geostatistical inversion: well −logs+AI+seismic data
Changes in end-point water relative permeability (100% — perturbation)	$k^o_{rw}=0.3$	GF-1
	$k^o_{rw}=0.6$	GF-2
Imbibition capillary pressure curve	Brooks	GF-1
	Corey	GF-3

petrophysical, fluid, and rock-fluid properties on the simulated time records of fluid production, compared to the influence of spatial variations of porosity and permeability.

8. Conclusions

The following is an itemized list of the most important conclusions stemming from this study:

(1) For the study considered in this paper, we found that the use of seismic amplitudes for estimating inter-well porosity and permeability had a substantial positive impact on the prediction of fluid production with time. We showed that uncertainty and bias in the prediction of reservoir production drastically decreased with the use of post-stack seismic amplitude data when constructing the static reservoir model.
(2) Reservoir distributions of porosity and permeability constructed with geostatistical inversion entailed the most accurate and least biased predictions of reservoir production when compared to predictions performed with conventional geostatistical simulation techniques.
(3) Extensive sensitivity analyses of all the variables and parameters involved in the interpolation of inter-well porosity and permeability indicated that geostatistical inversion is a more reliable alternative to conventional SGS and CSGS reservoir construction methods when there are only a few wells available for reservoir description.
(4) For the reservoir under consideration, the spatial continuity of permeability exhibited the largest influence on the behavior of fluid production and pressure depletion with time. Also, we found that perturbations to the relationship between porosity, permeability, and acoustic impedance produced significant variations in the simulated time record of fluid production.
(5) For the study under consideration, the degree of spatial variability of porosity and permeability was more significant than the degree of variation of rock-fluid properties (water relative permeability, and capillary pressure) in predicting reservoir production with time.
(6) The methodology considered in this paper to construct spatial distributions of porosity and permeability would be difficult, if not impossible to implement in thin-layer, and low-porosity reservoirs where seismic amplitudes do not uniquely respond to porosity and permeability. Also, a high degree of uncertainty in the relationship between seismic amplitudes and porosity and permeability could exist in shaly and low-porosity sands where variations of seismic-inverted acoustic impedance alone cannot be uniquely associated with variations of porosity, permeability, shale volume, fluid saturation, and reservoir thickness. For such cases, we recommend to perform a preliminary feasibility analysis based on a few wells within a small section of the area under consideration to quantify the relative benefits of honoring the seismic amplitude data in the construction of the corresponding reservoir models.

Acknowledgements

The authors wish to express their appreciation to UNOCAL Corporation for releasing to us the data set reported in this paper. A special note of gratitude goes to Fugro-Jason and Schlumberger for their generous donation of the software used to carry out trace-based inversion (Fugro-Jason), geostatistical inversion (Fugro-Jason), and multi-phase flow simulations (Schlumberger). The work reported in this paper was partially funded by UT Austin's Research Consortium on Formation Evaluation, jointly sponsored by Anadarko Petroleum Corporation, Baker Atlas, ConocoPhillips, ExxonMobil, Halliburton, the Mexican Institute for Petroleum, Schlumberger, Shell International E&P, and TOTAL. The Schlumberger Foundation provided partial support to Maika Gambús-Ordaz in the form of a fellowship.

References

Balan, B., Mohaghegh, S., Ameri, S., 1995. State-of-the-art in permeability determination from well log data: Part-1 a comparative study, model development: SPE No. 30978 presented at the Eastern Regional Conference and Exhibition, Morgantown, West Virginia.
Bashore, W., Araktingi, U., Levy, M., Schweller, W., 1993. The importance of the geological model for reservoir characterization using geostatistical techniques and the impact on subsequent fluid flow: SPE No. 26474 presented at the 68th Annual Technical Conference and Exhibition of the Society of Petroleum Engineers held in Houston, Texas.
Bassiouni, Z., 1994. Theory, Measurement, and Interpretation of Well Logs: SPE Textbook Series, vol. 4.
Box, G., Jenkins, G., Reinsel, G., 1994. Time Series Analysis. Prentice Hall.
Brooks, R., Corey, A., 1966. Properties of porous media effecting fluid flow: journal of irrigation drainage. Div. Am. Soc. Civil Eng. 92 (IR2), 61–88.
Castagna, J., Backus, M., 1993. Offset Dependent Reflectivity - Theory and Practice of AVO Analysis. Society of Exploration Geophysicists.
Debeye, H., Van Riel, P., 1990. Lp-norm deconvolution. Geophys. Prospect. 38, 381–403.
Deutsch, C., Journel, A., 1998. GSLIB, Geostatistical Software Library and User's Guide. Oxford University Press.
Gambús, M., Torres-Verdín, C., 2002. High-resolution geostatistical inversion of a 3D seismic data set acquired in a Gulf of Mexico gas field. 72nd Annual Technical Conference and Exhibition, SEG, Expanded Abstracts.
Gambús, M., 2005, A field study to assess the value of 3D post-stack seismic data in forecasting fluid production from a deepwater Gulf of Mexico reservoir: Ph.D. Dissertation, The University of Texas at Austin.
Grijalba-Cuenca, A., Torres-Verdín, C., Debeye, H., 2000. Geostatistical inversion of 3D seismic data to extrapolate wireline petrophysical variables laterally away from the well: SPE No. 63283 presented at the Annual International Technical Conference, Dallas, Texas.
Haas, A., Dubrule, O., 1994. Geostatistical inversion: a sequential method for stochastic reservoir modeling constrained by seismic data. First Break 12, 561–569.
Journel, A., Huijbregts, C., 1978. Mining Geostatistics. Academic Press Inc.
Landa, J., Horne, R., 1997. A procedure to integrate well test data, reservoir performance history and 4-D seismic information into a reservoir description: SPE No. 38653 presented at the SPE Annual Technical Conference and Exhibition held in San Antonio, Texas.
Landa, J., Guyaguler, B., 2003. A methodology of history matching and the assessment of uncertainties associated with flow prediction: SPE No. 84465 presented at the SPE Annual Technical Conference and Exhibition held in Denver, Colorado.
Lortzer, G., Berkhout, A., 1992. An integrated approach to lithologic inversion – Part 1. Geophysics 57, 233–245.
Pendrel, J., Van Riel, P., 1997. Estimating porosity from 3D seismic inversion and 3D geostatistics: Presented at the 67th Annual International Meeting, SEG.
Varela, O., Torres-Verdín, C., Lake, L., 2002. Assessing the value of 3D seismic data in reducing uncertainty in reservoir production forecasts: SPE No. 77359 presented at the SPE Annual Technical Conference and Exhibition, San Antonio, Texas.
Walsh, P., Lake, L., 2003. A Generalized Approach to Primary Hydrocarbon Recovery. Elsevier Publications.